



**HAL**  
open science

# Enhancement of a Gauss-Newton reconstruction for an inhomogeneous refraction index through defects localization

Yann Grisel, Jean-Pierre Raymond, Pierre-Alain Mazet, Vincent Mouysset

► **To cite this version:**

Yann Grisel, Jean-Pierre Raymond, Pierre-Alain Mazet, Vincent Mouysset. Enhancement of a Gauss-Newton reconstruction for an inhomogeneous refraction index through defects localization. 2013. hal-00814331v1

**HAL Id: hal-00814331**

**<https://hal.science/hal-00814331v1>**

Preprint submitted on 16 Apr 2013 (v1), last revised 12 Nov 2014 (v4)

**HAL** is a multi-disciplinary open access archive for the deposit and dissemination of scientific research documents, whether they are published or not. The documents may come from teaching and research institutions in France or abroad, or from public or private research centers.

L'archive ouverte pluridisciplinaire **HAL**, est destinée au dépôt et à la diffusion de documents scientifiques de niveau recherche, publiés ou non, émanant des établissements d'enseignement et de recherche français ou étrangers, des laboratoires publics ou privés.

# Enhancement of a Gauss-Newton reconstruction for an inhomogeneous refraction index through defects localization

Support for some of the authors of this work was provided by the FRAE (Fondation de Recherche pour l'Aéronautique et l'Espace, <http://www.fnrae.org/>), research project IPPON.

YANN GRISEL, JEAN-PIERRE RAYMOND,

Université Paul Sabatier, Institut de Mathématiques de Toulouse, 31062 Toulouse, France

PIERRE-ALAIN MAZET AND VINCENT MOUYSSET

Onera - The French Aerospace Lab, 31055 Toulouse, France

(Communicated by the associate editor name)

This paper deals with the reconstruction of both the internal geometry and the values of an inhomogeneous acoustic refraction index through a piece-wise constant iterative approximation. We propose to enhance a classical Gauss-Newton scheme through the use of geometrical informations gained from a previously developed defects localization method. Both enhancements are aimed to reducing the number of computed parameters. The first one consists in a preliminary selection of relevant parameters, while the second one is an adaptive refinement to enhance precision with a low number of parameters. Each of them is numerically illustrated.

## 1 Introduction

We consider the inverse medium problem consisting in the reconstruction of an inhomogeneous acoustic refraction index from far-field measurements generated through plane waves. The inverse medium problem is non-linear and ill-posed, which makes it difficult to solve [11]. Applications are, for example and among others, non-destructive structures testing or biomedical imaging [15, 17, 12].

Classically, the inverse medium problem is written as a least-squares problem and we will look for the index of refraction as a piece-wise constant function. We are thus in the context of non-linear and ill-posed parameter identification, which calls for specific methods. Among them, for its ease of implementation and efficiency for medium-sized problems, we consider the popular Gauss-Newton method applied to a Tykhonov regularized data misfit cost functional [8]. However, in its usual form, the Gauss-Newton method treats all parameters alike. Yet, during the reconstruction, or even right from the beginning, some parameters can reach an acceptable precision while the others still need to be updated to reach a global precision. In the absence of some local information, these acceptable parameters are then uselessly updated at each iteration. In this setting, we thus explore two uses of geometrical information, gained through defects localization, to focus the reconstruction and consequently lighten this inverse medium problem’s numerical resolution.

Defects are generally understood as perturbations with respect to some known reference. Conversely, this (known) reference can also be seen as an inexact estimation of the (unknown) perturbed state. It has recently been proved in [10] that the location of the defects in a given refraction index could be established from far-field measurements of the unknown state and computed through a fast numerical method. We propose here to use this fast local information to reduce the computation effort in the complete refraction index reconstruction process. Coupling between shape reconstruction and parameters identification has also been proposed by using the *Linear Sampling* method [5] in [4]. However, the *Factorization method* approach used [10] provides a more straightforward formulation as an equivalency that is defined at each point.

In a first time, we consider the case where a known index has been locally modified. This could happen, for instance, from a local deterioration or a partially incorrect estimation of the actual index. In this case, a preliminary defects localization provides a geometrical information that is which parameters have to be reconstructed. The reconstruction can then be performed straightforwardly on a reduced computational domain. In a second time, we investigate adaptive refinement. Here, defects localization is used to exhibit inaccurate regions in the current reconstruction. This local information allows us to add base functions in selected locations and resume the reconstruction to get a better precision while restraining the number of unknown parameters.

This paper is structured as follows: At first, section 2 specifies the mathematical setting. The direct problem is introduced in section 2.1 and followed in section 2.2 by the description of the inverse medium problem we are interested in. The numerical method on which we will build our enhancements is then described in section 2.3. Afterwards, the defects localization and its applications are presented in section 3. We show how to reduce the reconstruction domain in section 3.1 and the adaptive refinement process is detailed in section 3.2. Finally, we numerically illustrate the coupling of both applications, and also on a non-trivial example, in section 4 and conclude.

## 2 Presentation of the problem

We here introduce the inverse medium problem, followed by its numerical treatment and preceded by the direct problem.

### 2.1 The direct problem

If we consider time-harmonic acoustic waves with a fixed wave number  $k$ , the spatial part of the wave equation is modeled by the Helmholtz equation [6]. Inhomogeneous media are then represented by an acoustic refraction index, denoted by  $n \in L^\infty(\mathbb{R}^d)$ , and so, the total field, denoted by  $u_n \in L^2_{loc}(\mathbb{R}^d)$ , is assumed to satisfy

$$\Delta u_n + k^2 n(x) u_n = 0, \quad x \in \mathbb{R}^d, \quad (1)$$

where  $d$  is the problem's dimension ( $d = 2$  or  $3$ ). We consider compactly supported inhomogeneities and denote by  $D$  the support of  $n(x) - 1$ . Also, we denote an incoming wave satisfying (1) with  $n = 1$  by  $u^i \in L^2_{loc}(\mathbb{R}^d)$ . The total field is then the sum of this incoming wave and the wave scattered by the inhomogeneous medium, denoted by  $u^s \in L^2_{loc}(\mathbb{R}^d)$ :

$$u_n := u^s + u^i, \quad (2)$$

where the scattered wave is assumed to satisfy the Sommerfeld radiation condition

$$\partial_r u^s = iku^s + \mathcal{O}\left(|x|^{-\frac{d-1}{2}}\right). \quad (3)$$

Then, the linear system (1)-(3) defines  $u_n$  uniquely from  $u^i$ , and it is known to be invertible in  $L^2(D)$  [6, Chap. 8].

Besides, the outgoing part of a wave has an asymptotic behavior called the far field pattern, denoted by  $u_n^\infty \in \mathcal{C}^\infty(\Gamma_m)$  and given by the Atkinson expansion [19]

$$u_n(x) := u^i(x) + \gamma \frac{e^{ik|x|}}{|x|^{\frac{d-1}{2}}} u_n^\infty(\hat{x}) + \mathcal{O}\left(|x|^{-\frac{d-1}{2}}\right), \quad \hat{x} := \frac{x}{|x|} \in \Gamma_m, \quad (4)$$

where  $\Gamma_m$  denotes the set of measurement directions as a subset of the unit sphere  $S^{d-1}$  (see figure 1) and where  $\gamma$  depends only on the dimension and is defined by

$$\gamma := \begin{cases} \frac{e^{i\pi/4}}{\sqrt{8\pi k}} & \text{if } d = 2, \\ \frac{1}{4\pi} & \text{if } d = 3. \end{cases}$$

Furthermore, for practical reasons, we will mainly consider scattered waves having a plane-wave source. These plane-waves are defined by

$$u^i(\hat{\theta}, x) := \exp(ik\hat{\theta} \cdot x),$$

where  $\hat{\theta}$  is a unitary vector in the set of incidence directions, denoted by  $\Gamma_e$  as depicted on figure 1. We then denote the total field with a plane-wave source of incoming direction  $\hat{\theta}$  by

$$u_n(\hat{\theta}, x), \quad \hat{\theta} \in \Gamma_e, \quad x \in \mathbb{R}^d.$$

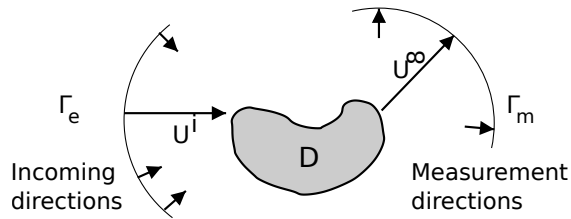


Figure 1: General setting and notations.

Lastly, the corresponding far-field pattern in the measurement direction  $\hat{x} \in \Gamma_m$  will be denoted by

$$u_n^\infty(\hat{\theta}, \hat{x}), \quad \hat{\theta} \in \Gamma_e, \hat{x} \in \Gamma_m.$$

## 2.2 The inverse medium problem

We are interested in the reconstruction, from far-field data, of an (unknown) inhomogeneous refraction index that will be denoted throughout this paper by  $n^* \in L^\infty(D)$ . All considered indices are implicitly extended by 1 outside  $D$ . We thus define the index-to-far-field mapping  $\mathcal{F} : L^\infty(D) \rightarrow \mathcal{C}^\infty(\Gamma_e \times \Gamma_m)$  by

$$\mathcal{F}(n) := u_n^\infty.$$

Besides, data are generally perturbed by noise or measurement errors and we only have access to  $\mathbf{u}^\varepsilon$  satisfying

$$\|\mathbf{u}^\varepsilon - u_{n^*}^\infty\|_{\mathcal{C}^\infty(\Gamma_e \times \Gamma_m)} \leq \varepsilon. \quad (5)$$

The usual approach to this problem is then to minimize the non-linear data misfit. However, most methods to solve this problem are set in Hilbert spaces, so we will have to consider  $\mathcal{F}$  as an application from  $L^2(D)$  into  $L^2(\Gamma_e \times \Gamma_m)$  and thus define the data misfit by

$$J(n) := c_1 \|\mathcal{F}(n) - \mathbf{u}^\varepsilon\|_{L^2(\Gamma_e \times \Gamma_m)}^2,$$

where  $c_1$  denotes a normalization constant (e.g.  $c_1 := \|\mathbf{u}^\varepsilon\|_{L^2(\Gamma_e \times \Gamma_m)}^{-2}$ ).

Even so, this problem is not continuous, as is shown by the following proposition. As such, even a small perturbation  $\varepsilon$  can lead to a minimizer very far from  $n^*$ .

**Proposition 1.** *The non-linear problem consisting in “finding  $n_\varepsilon$  minimizing  $J$ ” is ill-posed in the sense of Hadamard.*

*Proof.* The application  $\mathcal{F}$  is compact and thus cannot have a continuous inverse. Indeed, it has been shown that the total field  $u_n$  is bounded with respect to the  $L^\infty(D)$ -norm of  $n$  [16, Proposition 2.1.14]. As a consequence, the same holds for the mapping  $n \mapsto (n-1)u_n$ . Moreover, the asymptotic behavior of the Lippmann-Schwinger equation yields the following relation [6, Chap. 8.4]:

$$\mathcal{F}(n)(\hat{\theta}, \hat{x}) = \int_{z \in D} e^{-ik\hat{x} \cdot z} k^2 (n(z) - 1) u_n(\hat{\theta}, z), \quad \hat{\theta} \in \Gamma_e, \hat{x} \in \Gamma_m. \quad (6)$$

Hence, the non-linear operator  $\mathcal{F}$  is the combination of a linear compact operator with a continuous mapping and is thus compact itself.  $\square$

### 2.3 Iterative approximation by a piece-wise constant index

As stated in the introduction, we try to recover the unknown index  $n^*$  with help of piece-wise constant functions. Hence, the indices will numerically be represented by  $N$  complex parameters  $(\eta_i)_{i=1\dots N}$  associated to the same number of zones  $(Z_i)_{i=1\dots N}$ , so  $n(x) = \sum_{i=1\dots N} \eta_i \mathbf{1}_{Z_i}(x)$ . Each zone is thus a set of connected elements in the underlying mesh used to solve the Helmholtz equation. Moreover, to avoid any possibility of inverse crime, the reconstruction will be led on a different mesh than the one used to generate the data  $\mathbf{u}^\varepsilon$ . On this behalf, the respective supports of the basis functions associated to the unknown parameters will intersect the discontinuities of  $n^*$ . It is thus strictly impossible to reconstruct  $n^*$  exactly. This is illustrated on Figure 2, showing two 2D meshes that will be used our numerical examples.

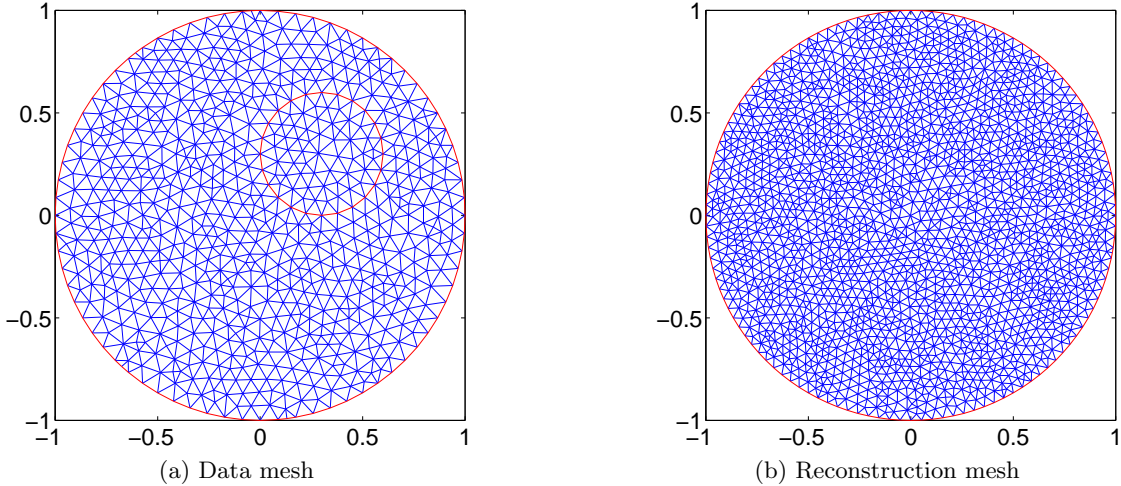


Figure 2: Test case geometry

In this setting, we use the well-known Gauss-Newton method applied to the cost function  $J$  with a standard Tikhonov regularization term [13]:

$$\tilde{J}(n) := c_1 \|\mathcal{F}(n) - \mathbf{u}^\varepsilon\|_{L^2(\Gamma_e \times \Gamma_m)}^2 + c_2 \|n - n_0\|_{L^2(D)}^2,$$

where  $c_2 > 0$  is a regularization parameter and  $n_0 \in L^2(D)$  is an initial guess. Assumptions on  $n_0$  and  $c_2$  for this method to converge are discussed in [1, 3]. The sought-for index  $n^*$  is hence approximated by a sequence  $(n_p)_{p \in \mathbb{N}}$  of indices, defined iteratively through Algorithm 1.

Moreover, we consider small enough amounts of data and unknown parameters to be able to compute the cost function's gradient in a reasonably fast time on a standard desktop computer. This gradient has the following simple formulation.

**Input:**  $n_0 \in L^2(D)$   
**1**  $p \leftarrow 0$ ;  
**2 repeat**  
**3**    Compute  $n_{p+1}$  by solving the linear system  

$$(D\mathcal{F}(n_p)^* D\mathcal{F}(n_p) + \frac{c_2}{2c_1} id)(n_{p+1} - n_0) =$$

$$-D\mathcal{F}(n_p)^*(\mathcal{F}(n_p) - \mathbf{u}^\varepsilon - D\mathcal{F}(n_p)(n_p - n_0)),$$
where  $id$  stands for the identity matrix;  
**4**     $p \leftarrow p + 1$ ;  
**5 until**  $\|n_p - n_{p-1}\|_2 / (1 + \|n_{p-1}\|_2) < \epsilon$ ;  
**Output:**  $n_{p_{\text{End}}}$

**Algorithm 1:** The Gauss-Newton method for  $\tilde{J}$

**Lemma 2.1.** *The application  $\mathcal{F}$  is twice differentiable. Moreover, the differential  $D\mathcal{F}$  evaluated at  $n \in L^\infty(D)$  and applied to the direction  $dn \in L^\infty(D)$  has the following integral representation*

$$D\mathcal{F}(n) dn : (\hat{\theta}, \hat{x}) \mapsto \int_{z \in D} k^2 u_n(-\hat{x}, z) u_n(\hat{\theta}, z) dn(z) dz, \quad \hat{\theta} \in \Gamma_e, \hat{x} \in \Gamma_m. \quad (7)$$

*Proof.* Expansion (4) shows that  $u_n^\infty(\hat{\theta}, \cdot)$  is linear with respect to the scattered field  $(u_n - u^i)(\hat{\theta}, \cdot)$ . Furthermore, It has been shown in [16, Proposition 4.3.1] that the scattered field is twice differentiable with respect to  $n$  and that the differential of the index-to-scattered-field mapping evaluated at  $n \in L^\infty(D)$ , applied to  $dn \in L^\infty(D)$ , is the function  $v^s(\hat{\theta}, \cdot) \in L_{loc}^2(\mathbb{R}^d)$  satisfying

$$(\Delta_x + k^2 n(x)) v^s(\hat{\theta}, x) = -k^2 u_n(\hat{\theta}, x) dn(x), \quad x \in \mathbb{R}^d, \quad (8)$$

and the Sommerfeld radiation condition. Note that, contrary to  $n$ , the direction  $dn$  is extended by 0 outside  $D$ . Thus,  $\mathcal{F}$  is twice differentiable and its differential is defined on  $\mathcal{C}^\infty(\Gamma_e \times \Gamma_m)$  by  $D\mathcal{F}(n) dn = v^\infty$ .

Now, note  $\Phi_n(z, x)$  the Green function to the Helmholtz equation (1). Multiplying (8) by  $\Phi_n(z, x)$ , integrating over  $D$  and using Green's formula then yields

$$v^s(\hat{\theta}, x) = \int_{z \in D} k^2 \Phi_n(z, x) u_n(\hat{\theta}, z) dn(z) dz, \quad x \in \mathbb{R}^d.$$

The asymptotic behavior is then given by

$$v^\infty(\hat{\theta}, \hat{x}) = \int_{z \in D} k^2 \Phi_n^\infty(z, \hat{x}) u_n(\hat{\theta}, z) dn(z) dz, \quad \hat{x} \in S^{d-1}.$$

Finally, representation (7) is obtained by applying the mixed reciprocity principle:  $\Phi_n^\infty(z, \hat{x}) = u_n(-\hat{x}, z)$  (see [14, equation (3.66)]).  $\square$

## Numerical example

To illustrate our reconstruction schemes in  $\mathbb{R}^2$ , we consider a disc  $D$  of radius 1 centered on the origin. The embedded perturbation  $\Omega$  is then another disc, this time centered on  $(0.3, 0.3)$  and of radius 0.3, as depicted on Figure 2a. The (perturbed) index we are looking for is set to  $n^* := 1.3$  in  $D \setminus \Omega$  and  $n^* := 1.6$  in  $\Omega$  whereas the initial guess, corresponding to the last known state, is  $n_0 := 1.3$  in  $D$ .

The Gaus-Newton method is performed with the regularization parameter set to  $c_2 := 10^{-2}$ . Also, required Helmholtz equation's solutions are computed *via*  $P^1$  finite elements and cartesian Perfectly Matched Layers (PML) [7]. Lastly, the corresponding far-fields are evaluated through representation 6. For all these examples, the wave number is set to  $k = 5$  and the incoming/measurement direction's angles are equally spaced in  $[0, 2\pi]$ .

An example can be seen on Figure 3 with the reconstruction mesh's 2672 triangles (see Figure 2b) divided into  $N = 10$ ,  $N = 27$ ,  $N = 75$  and  $N = 2672$  zones. For comparison purpose, we also list in Table 1 the exact final relative error

$$e_{p_{\text{End}}} := \|n_{p_{\text{End}}} - n^*\|_{L^2(D)} / \|n^*\|_{L^2(D)}$$

obtained in several configurations. Besides, we see in this table that the relative error is in the order of  $10^{-3}$ , so we set the stopping criterion to  $\epsilon = 10^{-4}$  for all our reconstructions.

N	$\epsilon$	15 × 15 data		30 × 30 data		60 × 60 data	
		$p_{\text{End}}$	$e_{p_{\text{End}}}$	$p_{\text{End}}$	$e_{p_{\text{End}}}$	$p_{\text{End}}$	$e_{p_{\text{End}}}$
10	5%	4	6.0%	4	5.9%	4	5.9%
	2%	4	5.9%	4	5.9%	4	5.8%
	1%	4	5.9%	4	5.9%	4	5.8%
27	5%	4	4.9%	4	4.9%	4	4.9%
	2%	4	4.9%	4	4.8%	4	4.8%
	1%	4	4.9%	4	4.8%	4	4.8%
75	5%	4	5.2%	4	4.4%	4	4.4%
	2%	4	3.8%	4	3.7%	4	3.7%
	1%	4	3.7%	4	3.6%	4	3.6%
2672	5%	4	4.6%	4	4.0%	4	4.4%
	2%	4	3.3%	4	3.2%	4	3.0%
	1%	4	3.0%	4	3.0%	4	3.0%

Table 1: Gauss Newton reconstruction



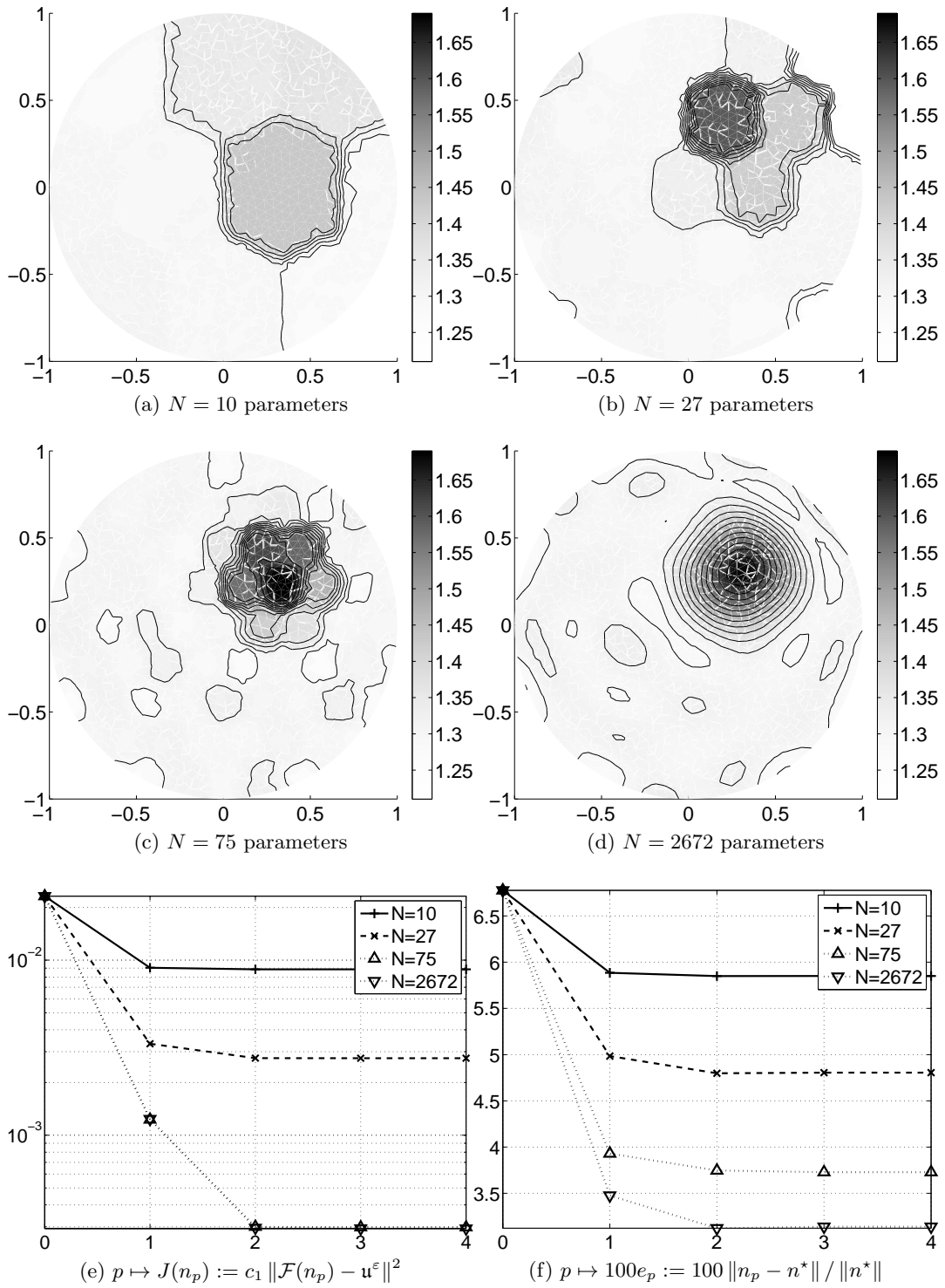


Figure 3: Gauss-Newton reconstruction with  $30 \times 30$  data and 2% noise

### 3 Enhancements of the Gauss-Newton method via defects localization

In the presented piece-wise constant iterative approximation, the possible precision is directly linked to the number of parameters  $N$  which, in turn, is linked to the computational effort. In the lack of some geometrical information, all constants are equally treated and updated at each iteration. In some cases however, this can generate more effort than is really needed and we address two of them.

1. For the first case, we place ourselves in the context of a localized perturbation of an otherwise known initial state  $n_0$ . So, one can state that most of the index has not changed and should not be reconstructed.
2. For the second case, we are concerned in focusing on the most inexact constants during the reconstruction. Indeed, to obtain a precise identification, the reconstruction mesh has to be refined in the zones intersected by the discontinuities of  $n^*$ . However, if  $n^*$  is constant in large areas, refining the reconstruction mesh everywhere only raises the computational effort for a relatively small precision increment.

To address these aspects of the reconstruction, the useful information in both cases would thus be the localization of the exact (enough) constants. Of course, to enhance the complete reconstruction, access to this specific information should be fast. To this end, it has been shown that there exist a defects localization function recalled in the following theorem.

**Theorem 3.1.** [10, Theorem 6.1] *Assume  $\Gamma_m = \Gamma_e = S^{d-1}$ . Then, define  $W := (Id + 2ik|\gamma|^2 F_n)(F_{n^*} - F_n)$ , where  $F_n : L^2(S^{d-1}) \rightarrow L^2(S^{d-1})$  denotes the classical far-field operator, defined by  $F_n g(\hat{x}) := \langle g, \overline{u_n^\infty(\cdot, \hat{x})} \rangle_{L^2(S^{d-1})}$ . Next, we define the positive self-adjoint operator  $W_\#$  by  $W_\# := |W + W^*| + |W - W^*|$ , where the notation  $|\cdot|$  applied to an operator  $L$  stands for  $|L| := (L^*L)^{\frac{1}{2}}$ . Lastly, assume that  $n$  and  $n^*$  are real valued and that either  $(n - n^*)$  or  $(n^* - n)$  is locally bounded from below on  $\Omega := \text{support}(n - n^*)$ . Then, for each  $z \in \mathbb{R}^d$ , we have*

$$n(z) \neq n^*(z) \iff \mathcal{S}_{\{n, n^*\}}(z) := \left( \sum_j \frac{|\langle \overline{u_n(\cdot, z)}, \psi_j \rangle_{L^2(S^{d-1})}|^2}{\sigma_j} \right)^{-1} > 0,$$

where  $(\sigma_j, \psi_j)$  is an eigensystem of  $W_\#$ .

**Remark 1.** As it is, this theorem requires full bi-static data and real-valued indices. However, we also recall the conjecture, stated in [10, Remark 6.2], that the same result could be obtained by defining the localization function  $\mathcal{S}$  with  $(\sigma_j, \psi_j)$  a right-singular system of  $(F_{n^*} - F_n)$ . The main benefit is the possibility to consider  $\Gamma_m \neq \Gamma_e \neq S^{d-1}$  and complex valued indices.

Furthermore, numerical examples in [10] seem to indicate that this localization is effective for defects bigger than (approximately) one sixth of the wavelength. Besides, in order to get satisfactory results in the successive resolutions of the Helmholtz equation, we have set the average reconstruction mesh element's size to be about one twentieth of the wavelength. Thus, we will only consider defects that cover at least four connected mesh elements.

Finally, the examples shown in [10] exhibit that defects can be located even when the surrounding background is not precisely known. Practically, low amplitude inaccuracies with respect to the exact index do not seem to interfere with the localization of the contrasting defects. Thus, geometrical information gained through the defects localization presented here is expected to focus on the most "defective" zones.

### 3.1 Selective reconstruction

We here consider the case where the initial guess  $n_0$  is exact, except for some perturbation whose support will be denoted by  $\Omega$ . Thus, we propose to perform a preliminary selection of the parameters that do need to be reconstructed. The whole index  $n^*$  is then reconstructed by updating those parameters only. This should generally lead to a reconstruction using significantly less parameters, summarized in Algorithm 2.

- Input:**  $n_0 \in L^2(D)$
- 1  $\mathcal{S}_i \leftarrow \max_{Z_i} \mathcal{S}_{\{n_0, n^*\}}(x)$ ;
  - 2  $\Omega_{\mathcal{T}} \leftarrow$  the set of zones for which  $\mathcal{S}_i > \mathcal{T} \max(\mathcal{S}_i)$ ;
  - 3  $n_{p_{\text{End}}} \leftarrow$  Algorithm 1( $n_0|_{\Omega_{\mathcal{T}}}$ ) (all indices are extended by  $n_0$  outside  $\Omega_{\mathcal{T}}$ );
- Output:**  $n_{p_{\text{End}}}$

**Algorithm 2:** Selective reconstruction

### Numerical example

In the framework of section 2.3, we here use one parameter for each reconstruction mesh element. Figure 4 shows which parameters are selected with three threshold values  $\mathcal{T} = 10\%$ ,  $\mathcal{T} = 20\%$  and  $\mathcal{T} = 30\%$ . We can see that a threshold of  $\mathcal{T} = 10\%$  selects slightly too much mesh elements and thus provides a satisfactory reconstruction with only 316 parameters. This is significantly less than the initial 2672 and thus, reaches the set goal. More precisely, we can see in Table 2 that the precision is superior to what was obtained through a full Gauss-Newton reconstruction. This was to be expected since, in the present case, all parameters outside the perturbation stay fixed to the exact value, where they can be misvaluated in the full reconstruction.

However, a threshold of  $\mathcal{T} = 20\%$  seems too high, as the 178 selected parameters do not completely cover the perturbation's support, resulting in a slightly flawed reconstruction. This brings up the problem, arising with every adjustable parameter, of how to select a correct threshold, depending at least on the measurements noise and the amount of

data. Unfortunately, for the moment, we do not have a reliable indicator to tell if the selected threshold was acceptable.

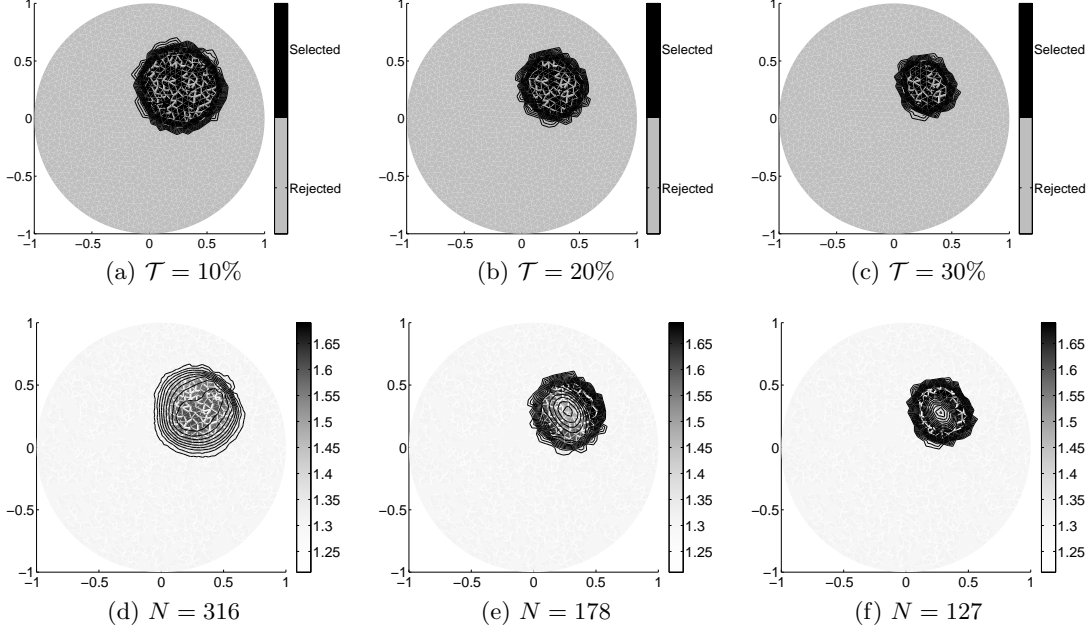


Figure 4: Selective reconstruction with  $30 \times 30$  data and 2% noise

### 3.2 Adaptive refinement

As stated in section 2.3, since we use a reconstruction mesh that is different from the one used to generate the data, these zones will most likely intersect discontinuities of  $n^*$ . Even more so with a low number of zones  $N$ . Thus, we propose to iteratively refine the reconstruction mesh with help of the previously introduced defects localization, in order to provide a satisfying approximation of the unknown index with a small number of parameters. The refinement's outline is presented in Algorithm 3.

The number of 16 mesh elements is taken so that, after the splitting, each zone still has more than four elements, which is the lower limit for defects to be relevant, as specified in Remark 1.

#### Numerical example

In the same conditions as before, we illustrate our adaptive refinement on Figure 5. Figures 5a–5h depict alternately steps 3 and 9 of Algorithm 3 and show how the reconstruction focuses on the contrasting perturbation's support. Figure 5i represents the values of  $n_{42}$ , which is obtained with  $N = 46$  parameters placed during 15 successive adaptive refinements. Also, the relative error  $e_p$ , obtained in step 10 of the algorithm, is plotted on Figure 5j as a function of  $p$ .

$\mathcal{T}$	$\varepsilon$	15 × 15 data			30 × 30 data			60 × 60 data		
		N	$p_{\text{End}}$	$e_{p_{\text{End}}}$	N	$p_{\text{End}}$	$e_{p_{\text{End}}}$	N	$p_{\text{End}}$	$e_{p_{\text{End}}}$
10%	5%	661	4	3.3%	730	4	3.0%	689	4	3.0%
	2%	328	4	2.3%	316	4	2.4%	333	4	2.3%
	1%	303	4	2.3%	323	4	2.3%	288	4	2.5%
20%	5%	288	4	2.7%	276	4	2.5%	282	4	2.7%
	2%	184	4	3.8%	178	4	3.8%	186	4	3.7%
	1%	175	4	3.9%	182	4	3.6%	168	4	4.1%
30%	5%	183	4	3.8%	185	4	3.6%	187	4	3.7%
	2%	128	4	5.5%	127	4	5.5%	128	4	5.5%
	1%	122	4	5.7%	129	4	5.5%	113	4	5.9%

Table 2: Selective reconstruction

**Input:**  $n_0 \in L^2(D)$

- 1  $p \leftarrow 0$ ;
- 2 **repeat**
- 3    $\mathcal{S}_i \leftarrow \max_{Z_i} \mathcal{S}_{\{n_p, n^*\}}(x)$ ;
- 4    $I \leftarrow \{i \text{ such that } Z_i \text{ contains more than 16 mesh elements}\}$ ;
- 5    $i_{\text{Split}} \leftarrow i \text{ such that } \mathcal{S}_{i_{\text{Split}}} = \max_{i \in I} \mathcal{S}_i$ ;
- 6   Update the set of zones by splitting  $Z_{i_{\text{Split}}}$  into four sub-zones;
- 7   Update the set of parameters accordingly by duplicating  $\eta_{i_{\text{Split}}}$  three times;
- 8    $N \leftarrow N + 3$ ;
- 9    $n_{p+p_{\text{End}}} \leftarrow \text{Algorithm 1}(n_p)$ ;
- 10    $p \leftarrow p + p_{\text{End}}$ ;
- 11 **until**  $N > N_{\text{max}}$  or each  $Z_i$  contains less than 16 mesh elements;

**Output:**  $n_{p_{\text{End}}}$

**Algorithm 3:** Adaptive refinement

Comparing with the relative errors listed in Table 1, or on Figure 3f, we can see that the guided adaptive refinement achieves better results than randomly placed basis functions. This example shows results even comparable to the full reconstruction with 20 times more parameters. It thus pictures a satisfactory reconstruction with a limited number of well-placed parameters.

These results present sensitivities to noise or data amount that go in the same lines as the previous examples, as can be seen in Table 3.

$\varepsilon$	15 × 15 data			30 × 30 data			60 × 60 data		
	N	$p_{\text{End}}$	$e_{p_{\text{End}}}$	N	$p_{\text{End}}$	$e_{p_{\text{End}}}$	N	$p_{\text{End}}$	$e_{p_{\text{End}}}$
5%	76	76	5.2%	76	66	4.4%	76	64	3.6%
2%	76	60	4.0%	76	59	3.9%	76	61	3.1%
1%	76	59	3.7%	76	60	3.5%	76	59	3.5%

Table 3: Adaptive refinement

## 4 Combining both strategies

The selective reconstruction is presented in section 3.1 as a preliminary step to the reconstruction. It can thus be followed by the adaptive refinement described in section 3.2. So, we further illustrate selective reconstruction and adaptive refinement by chaining them, as described in Algorithm 4.

- Input:**  $n_0 \in L^2(D)$
- 1  $\mathcal{S}_i \leftarrow \max_{Z_i} \mathcal{S}_{\{n_0, n^*\}}(x)$ ;
  - 2  $\Omega_{\mathcal{T}} \leftarrow$  the set of zones for which  $\mathcal{S}_i > \mathcal{T} \max(\mathcal{S}_i)$ ;
  - 3  $n_{p_{\text{End}}} \leftarrow$  Algorithm 3( $n_0|_{\Omega_{\mathcal{T}}}$ ) (all indices are extended by  $n_0$  outside  $\Omega_{\mathcal{T}}$ );
- Output:**  $n_{p_{\text{End}}}$

**Algorithm 4:** Selective reconstruction followed by adaptive refinement

### Numerical example 1

In line with section 3, we illustrate Algorithm 4 with the selection thresholds  $\mathcal{T} = 10\%$ ,  $\mathcal{T} = 20\%$  and  $\mathcal{T} = 30\%$ . The respective selected mesh elements can be seen on Figures 4a–4c. Figures 6a–6c show the reconstructions after 2, 3 and 17 adaptive refinement loops with a threshold  $\mathcal{T} = 10\%$ . As expected, since we already saw that the whole perturbation is captured, the result is a good reconstruction. In fact, the exact values listed in Table 4 show that this reconstruction achieves a precision in par with the results obtained through the initial selective reconstruction with about 10 times more basis functions.

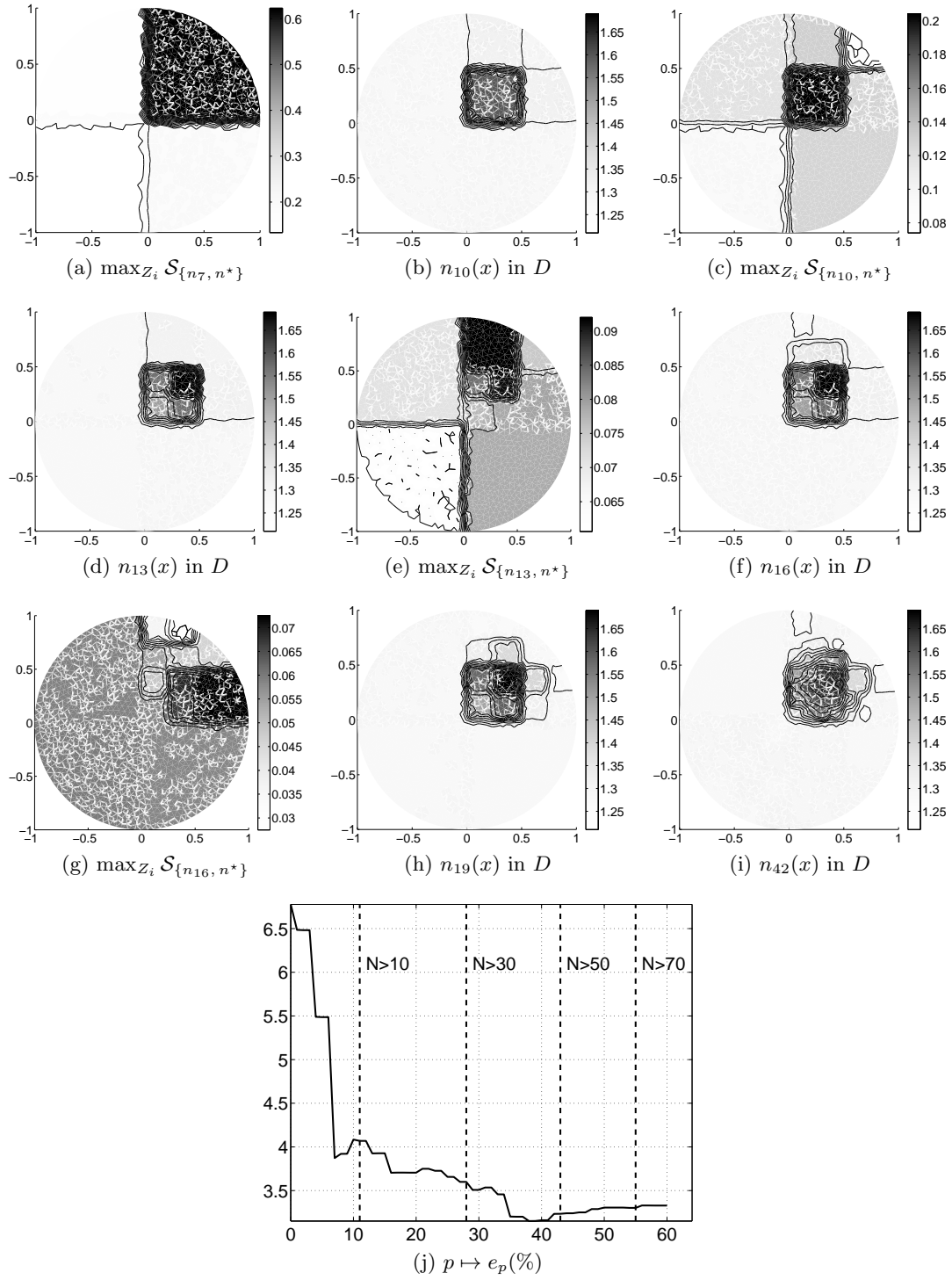


Figure 5: Adaptive refinement with  $30 \times 30$  data and 2% noise

Moreover, again similarly to the examples presented in section 3.1,  $\mathcal{T} \geq 20\%$  results in a too small selection, leading to a flawed reconstruction. It can be seen on Figures 6d–6i that the reconstruction tends to a crown shape. The corresponding relative error values are presented on Figure 6j and detailed in Table 4.

$\mathcal{T}$	$\varepsilon$	$15 \times 15$ data			$30 \times 30$ data			$60 \times 60$ data		
		N	$p_{\text{End}}$	$e_{p_{\text{End}}}$	N	$p_{\text{End}}$	$e_{p_{\text{End}}}$	N	$p_{\text{End}}$	$e_{p_{\text{End}}}$
10%	5%	74	69	4.8%	70	59	3.2%	69	63	3.3%
	2%	52	43	2.6%	52	45	2.5%	52	43	2.4%
	1%	52	44	2.5%	52	42	2.6%	52	41	2.6%
20%	5%	52	42	3.1%	52	41	2.7%	52	41	2.7%
	2%	16	19	4.1%	16	19	3.8%	19	21	3.5%
	1%	22	23	3.3%	16	19	4.2%	16	19	4.2%
30%	5%	16	19	4.6%	16	19	3.7%	19	21	3.6%
	2%	16	19	5.6%	16	19	5.6%	16	19	5.4%
	1%	15	19	5.2%	16	19	5.7%	16	19	5.7%

Table 4: Selective reconstruction chained with iterative refinement

## Numerical example 2

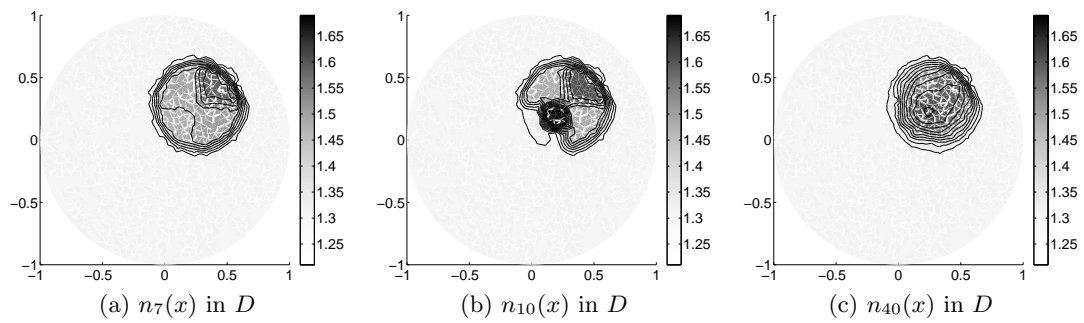
As a last example, we now consider a less trivial and complex valued unknown index  $n^*$ , shown on Figure 7. Besides, we also make this reconstruction more challenging by reducing the measurements aperture. The incoming directions are still taken in  $[0, 2\pi]$ , but there will be five less, and the measurement directions are now taken in  $[0, \frac{3}{2}\pi]$ . In this situation, the localization function presented in Theorem 3.1 can not be defined. So, we consider the technical modification recalled in Remark 1 that is conjectured to cover this case.

Furthermore, we assume that  $n^*$  was known previously to the central perturbation, which translates in the initial guess  $n_0$  depicted on Figure 8. The reference reconstructions obtained with Algorithm 1 are presented in Table 5.

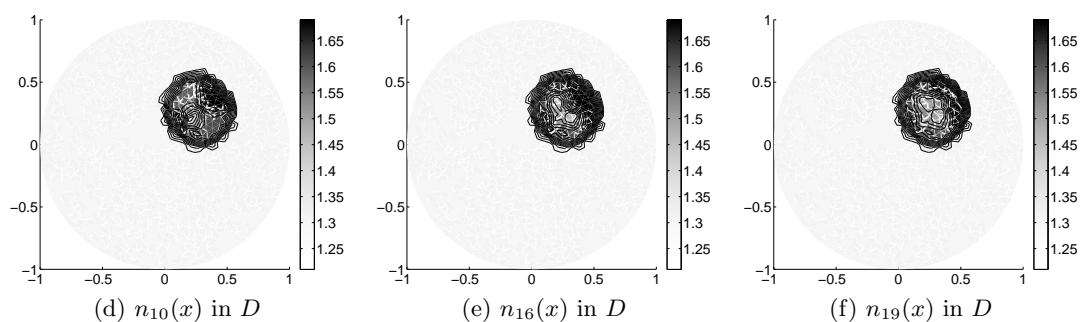
To remain in the previously defined context, we present the results of Algorithm 4 applied to this new geometry with the same thresholds  $\mathcal{T} = 10\%, 20\%$  and  $30\%$ . Figure 9 then depicts for each threshold the corresponding selected parameters and the resulting reconstruction. In this case,  $\mathcal{T} = 20\%$  now seems to be the best threshold value and  $\mathcal{T} = 30\%$  is still too high. This is confirmed on Figure 9j, where we can see that, even though  $\mathcal{T} = 10\%$  allows to reach a satisfying precision, it requires much more refinements to do so than with  $\mathcal{T} = 20\%$ . Also, more specific results for different simulated configurations are listed in Table 6.

The results obtained in section 3 are thus backed up by this example, exhibiting reconstructions comparable in precision to the full Gauss-Newton reconstruction, but with a much lower number of parameters.

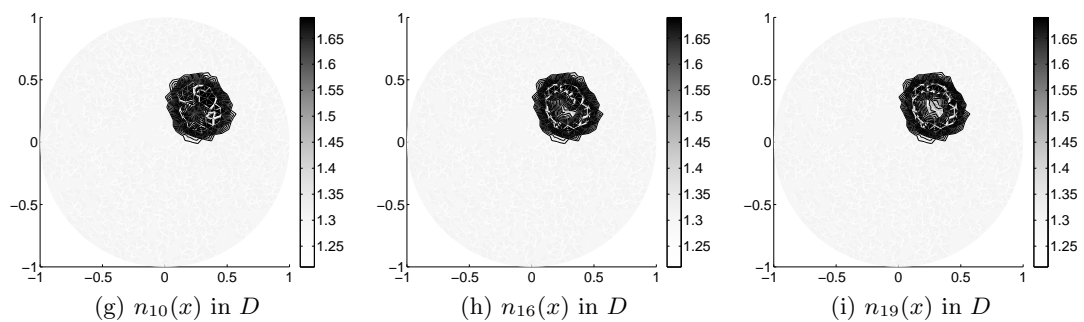




$\mathcal{T} = 10\%$



$\mathcal{T} = 20\%$



$\mathcal{T} = 30\%$

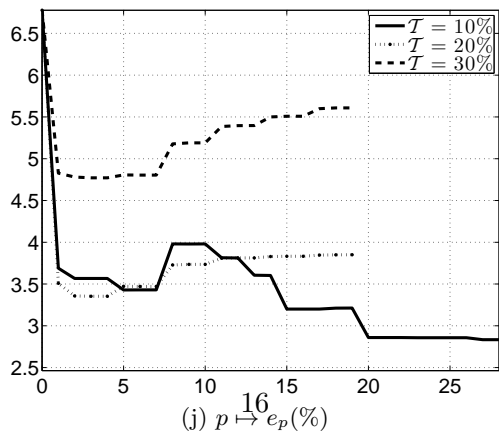


Figure 6: Selective reconstruction chained with adaptive refinement,  $30 \times 30$  data and 2% noise

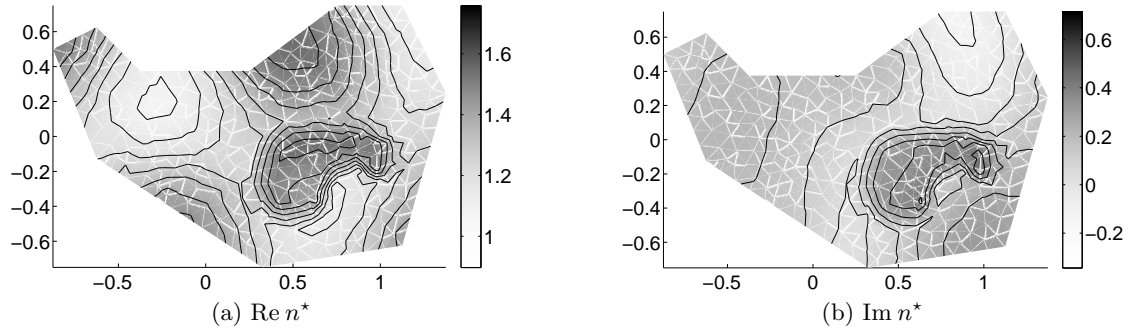


Figure 7: Exact index  $n^*$

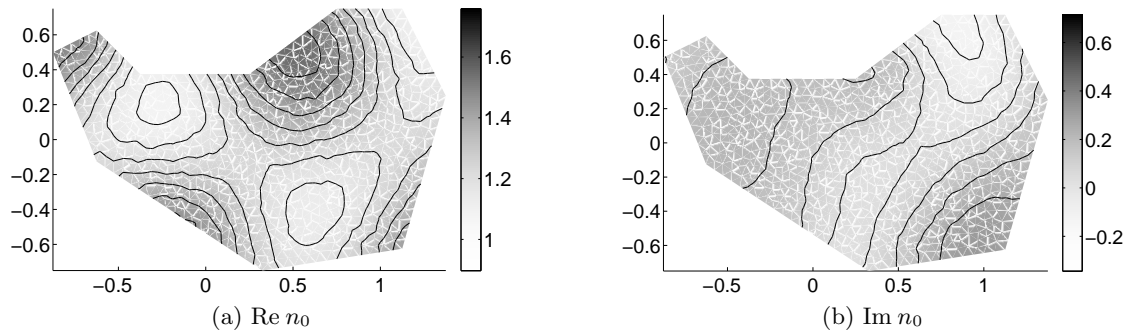
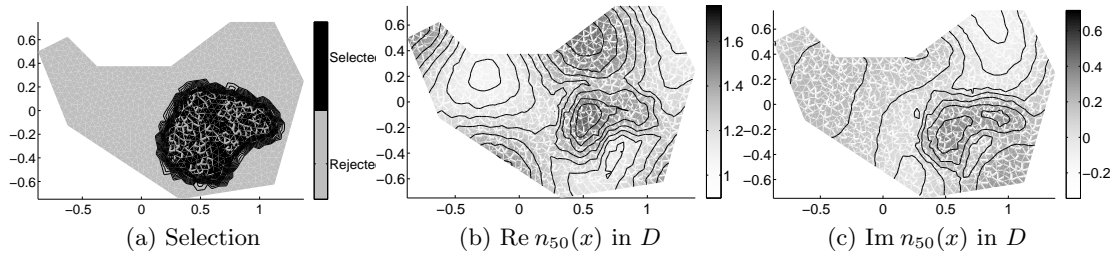


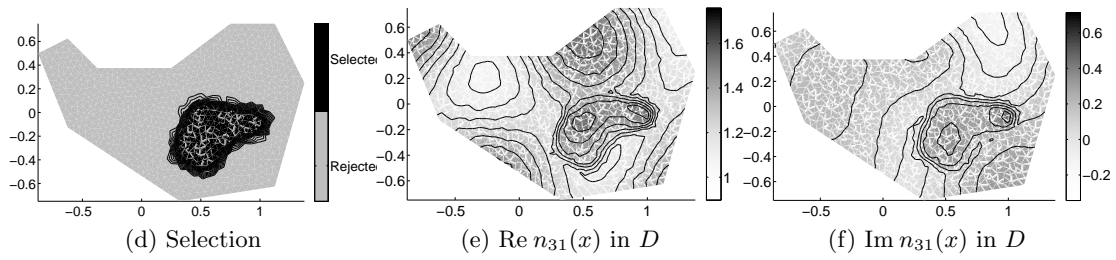
Figure 8: Initial guess  $n_0$

N	$\varepsilon$	10 × 15 data		25 × 30 data		55 × 60 data	
		$p_{\text{End}}$	$e_{p_{\text{End}}}$	$p_{\text{End}}$	$e_{p_{\text{End}}}$	$p_{\text{End}}$	$e_{p_{\text{End}}}$
10	5%	5	11.6%	5	11.6%	5	11.5%
	2%	5	11.6%	5	11.5%	5	11.5%
	1%	5	11.6%	5	11.5%	5	11.5%
23	5%	4	11.1%	4	10.7%	5	10.6%
	2%	4	10.5%	4	10.6%	5	10.4%
	1%	4	10.4%	5	10.4%	4	10.4%
64	5%	5	9.0%	5	8.4%	5	7.9%
	2%	5	7.7%	4	7.6%	5	7.6%
	1%	5	7.6%	5	7.5%	5	7.5%
1832	5%	5	7.8%	5	6.7%	5	6.2%
	2%	5	6.1%	5	6.0%	5	5.8%
	1%	5	5.9%	5	5.8%	5	5.8%

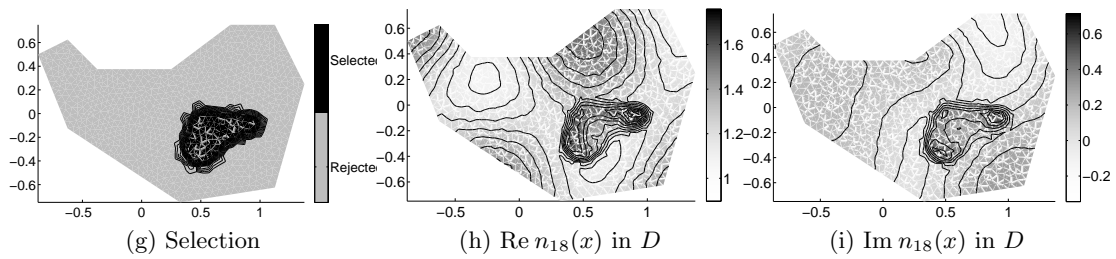
Table 5: Gauss Newton reconstruction for the more elaborate example



$\mathcal{T} = 10\%$



$\mathcal{T} = 20\%$



$\mathcal{T} = 30\%$

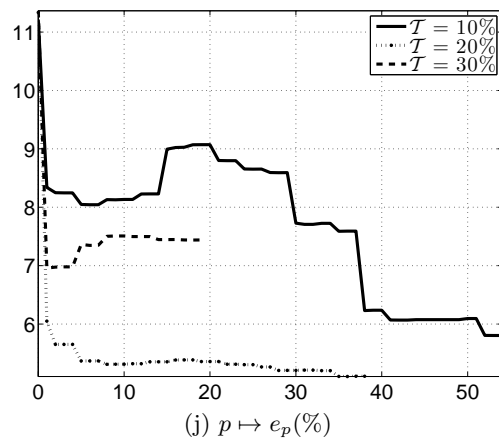


Figure 9: Selective reconstruction chained with adaptive refinement for the more elaborate example with  $30 \times 30$  data and 2% noise

$\mathcal{T}$	$\varepsilon$	10 × 15 data			25 × 30 data			55 × 60 data		
		N	$p_{\text{End}}$	$e_{p_{\text{End}}}$	N	$p_{\text{End}}$	$e_{p_{\text{End}}}$	N	$p_{\text{End}}$	$e_{p_{\text{End}}}$
0%	5%	76	95	12.6%	76	91	14.9%	76	86	10.2%
	2%	76	90	13.4%	76	84	9.6%	76	84	9.1%
	1%	76	93	11.9%	76	85	8.1%	76	84	8.1%
10%	5%	73	82	10.0%	75	76	6.3%	52	58	5.7%
	2%	57	62	5.9%	48	50	5.6%	48	50	5.5%
	1%	51	52	5.6%	48	47	5.5%	45	43	5.2%
20%	5%	51	53	5.7%	42	42	5.5%	45	42	5.7%
	2%	45	42	5.4%	34	31	5.7%	27	27	6.3%
	1%	40	35	5.3%	24	24	6.2%	13	17	7.8%
30%	5%	37	35	5.7%	28	26	6.4%	13	18	8.5%
	2%	25	25	6.5%	13	18	8.6%	13	18	9.2%
	1%	16	19	7.8%	13	18	8.9%	13	19	10.3%

Table 6: Selective reconstruction chained with adaptive refinement for the more elaborate example

## 5 Conclusion

We have used a previously developed defects localization method to propose two ways of reducing the number of parameters in the reconstruction on an unknown refraction index. The first method is set in the context of defects identification and uses their localization to reconstruct only the useful parameters of the whole index. The second method is an adaptive refinement, based on defects localization to iteratively reconstruct a better approximation with a contained number of parameters.

Both methods have shown good numerical results with the presented Gauss-Newton method. The reconstruction could however be further enhanced by two automations: some automatic thresholding for the defects localization function and some automatic selection of the regularization parameter. The second issue has been reviewed for example in [9, 2] and is claimed to be less critical when using a so-called Multiplicative Regularization described in [18]. However, to this point, we have not been able to further enhance our results with these techniques.

## References

- [1] A.B. Bakushinsky. The problem of the convergence of the iteratively regularized gauss-newton method. *Computational mathematics and mathematical physics*, 32(9):1353–1359, 1992.
- [2] Fermín S. Viloche Bazán and Juliano B. Francisco. An improved fixed-point al-

- gorithm for determining a Tikhonov regularization parameter. *Inverse Problems*, 25(4):045007, 16, 2009.
- [3] Barbara Blaschke, Andreas Neubauer, and Otmar Scherzer. On convergence rates for the iteratively regularized Gauss-Newton method. *IMA J. Numer. Anal.*, 17(3):421–436, 1997.
- [4] M. Brignone, G. Bozza, A. Randazzo, M. Piana, and M. Pastorino. A hybrid approach to 3d microwave imaging by using linear sampling and aco. *Antennas and Propagation, IEEE Transactions on*, 56(10):3224–3232, 2008.
- [5] D. Colton and A. Kirsch. A simple method for solving inverse scattering problems in the resonance region. *Inverse Problems*, 12(4):383–393, 1996.
- [6] D. Colton and R. Kress. *Inverse acoustic and electromagnetic scattering theory*, volume 93 of *Applied Mathematical Sciences*. Springer-Verlag, Berlin, second edition, 1998.
- [7] B. Dah. *Sur la modélisation de milieux fictifs absorbants de type couches de Bérenger*. PhD thesis, Université Toulouse III, 2001.
- [8] H.W. Engl, M. Hanke, and A. Neubauer. *Regularization of inverse problems*, volume 375. Springer Netherlands, 1996.
- [9] C.G. Farquharson and D.W. Oldenburg. A comparison of automatic techniques for estimating the regularization parameter in non-linear inverse problems. *Geophysical Journal International*, 156(3):411–425, 2004.
- [10] Y. Grisel, V. Mouysset, P-A. Mazet, and J-P. Raymond. Determining the shape of defects in non-absorbing inhomogeneous media from far-field measurements. *Inverse Problems*, 28:055003, 2012.
- [11] T. Hohage. On the numerical solution of a three-dimensional inverse medium scattering problem. *Inverse Problems*, 17(6):1743–1763, 2001.
- [12] P. Mojabi and J. LoVetri. Microwave biomedical imaging using the multiplicative regularized gauss-newton inversion. *Antennas and Wireless Propagation Letters, IEEE*, 8:645–648, 2009.
- [13] P. Mojabi and J. LoVetri. Overview and classification of some regularization techniques for the gauss-newton inversion method applied to inverse scattering problems. *Antennas and Propagation, IEEE Transactions on*, 57(9):2658–2665, 2009.
- [14] A. I. Nachman, L. Päivärinta, and A. Teirilä. On imaging obstacles inside inhomogeneous media. *J. Funct. Anal.*, 252(2):490–516, 2007.
- [15] I.G. Scott and C.M. Scala. A review of non-destructive testing of composite materials. *NDT International*, 15(2):75–86, 1982.

- [16] L. Ségui. *Sur un problème inverse en diffraction d'ondes : identification de permittivités complexes d'un matériau à partir de données du champ proche*. PhD thesis, Université Toulouse III, 2000.
- [17] L.P. Song, C. Yu, and Q.H. Liu. Through-wall imaging (twi) by radar: 2-d tomographic results and analyses. *Geoscience and Remote Sensing, IEEE Transactions on*, 43(12):2793–2798, 2005.
- [18] P. M. van den Berg, A. L. van Broekhoven, and A. Abubakar. Extended contrast source inversion. *Inverse Problems*, 15(5):1325–1344, 1999.
- [19] G. Venkov. Atkinson-Wilcox expansion theorem for inhomogeneous media. In *Math. Proc. R. Ir. Acad.*, volume 108, pages 19–25, 2008.

Received xxxx 20xx; revised xxxx 20xx.